# Thermally Optimized Chemical Vapor Deposition of Iron and Cobalt on Pd-Decorated Reduced Graphene Oxide for Atomic-Scale Catalytic Interface Engineering

*Samira Mehravar[1], Abbas Ali Khodadadi[1], Shohreh Fatemi[1], Yadollah Mortazavi[1*]*

[1]School of Chemical Engineering, College of Engineering, University of Tehran, P.O. Box 11155/4563, Tehran, Iran.

* Corresponding author

E-mail address: Mortazav@ut.ac.ir, Tel.: +98 21 6697793



**Abstract**

This study investigates the catalytic mechanisms underlying the chemical vapor deposition (CVD) of iron (Fe) and cobalt (Co) on palladium-decorated reduced graphene oxide (Pd/rGO) compared to bare rGO. Pd nanoparticles (~9.37 nm) on rGO significantly enhance precursor decomposition and catalyst formation. Temperature-resolved gas-phase Fourier-transform infrared (FTIR) spectroscopy tracked ferrocene and cobaltocene decomposition, revealing distinct optimal temperature windows—termed Frontier Thermal Bulwarks (FTBs)—for Fe (100–270 °C) and Co (40–140 °C) deposition. Pd/rGO exhibited earlier onset of gas-phase precursor decomposition (~100 °C for Fe and ~40 °C for Co) and higher C–H stretching band intensities than rGO, highlighting Pd's role in efficient $H_2$ dissociation and ligand activation. Unique spectral features, including 1037/1094 $cm^{-1}$ peaks for cobaltocene, correspond to specific intermediate species arising from its 19-electron instability. The selective CVD on Pd/rGO promotes intimate Fe/Co-Pd interactions, which may enhance catalytic performance while minimizing precious metal usage. These findings provide key insights for optimizing

CVD conditions in the development of advanced nanostructured catalysts for energy and environmental applications.

***Keywords:*** Palladium Nanoparticles, Ferrocene, Cobaltocene, Reduced Graphene Oxide, Selective Chemical Vapor Deposition; Gas-FTIR Monitoring.

## 1. Introduction

The development of Pd nanoparticles supported on transition metals such as Fe and Co has emerged as a powerful strategy for designing advanced nanostructured catalysts. These Pd–metal heterostructures offer high surface areas, tunable electronic properties, and robust interfacial interactions that synergistically enhance catalytic performance. [1], [2], [3] By facilitating hybrid active sites, introducing surface defects, and promoting effective electron and mass transport, these materials enable superior control over key catalytic reactions including oxidation,[4], [5] hydrogenation,[6], [7], [8] and Fischer-Tropsch synthesis. [9], [10]

Metallic Fe and Co bring distinct catalytic advantages. Fe is broadly investigated for its ability to modulate electronic states and induce oxygen vacancies, significantly improving reactivity in environmental catalysis, such as NOx reduction.[11], [12] Co exhibits versatile redox behavior via $Co^{2+}/Co^{3+}$ transitions, facilitating its critical role in electrochemical energy storage [13] and conversion technologies.[14] Integration of these metals with Pd not only enhances catalytic activity but also improves catalyst stability by mitigating sintering and poisoning effects, which is essential for scalable industrial applications. [15][16], [17] Furthermore, the catalytic efficacy of Pd can be significantly augmented through bimetallic synergy with Fe or Co, as these secondary metals reduce the HOMO–LUMO gap and stabilize the active sites, enabling efficient activation of inert C─H bonds under mild conditions for transformations such as C─C, C─O, C─X, and C─N bond formations.[18] This approach leverages Pd(II)-mediated C─H activation mechanisms, where the formation of organometallic intermediates facilitates selective functionalization, a strategy increasingly explored in the design of carbon-supported heterogeneous catalysts.[18]

Reduced graphene oxide (rGO) has emerged as a preferred support material due to its two-dimensional layered structure, exceptional electrical conductivity, and abundance of functional groups (e.g., hydroxyl, epoxy, carboxyl), which collectively enhance its versatility in catalytic applications. [19] These intrinsic properties facilitate robust anchoring and uniform dispersion of Pd, Fe, and Co nanoparticles, effectively mitigating particle aggregation while accelerating charge transfer kinetics, thereby optimizing catalytic efficiency.[20] Recent advancements have introduced a novel class of catalytic materials termed "GrafeoPlad," wherein graphene oxide is intricately entrapped within palladium nanoparticles, forming metal-organic hybrid structures that exhibit enhanced catalytic performance in heterogeneous reactions.[21] This innovative architecture leverages the synergistic interplay between rGO's structural framework and the catalytic activity of Pd, opening new avenues for reaction engineering.[22] Consequently, rGO-supported catalysts have demonstrated superior efficacy across a broad spectrum of applications, including electrochemical sensing and pollutant degradation. [23], [24], [25], [26]

Despite these advances, precise control over nanoparticle size, distribution, and atomic-level interfacial structure remains a key challenge due to the complex chemistry of metal precursors and their surface reactions. Vapor-phase deposition techniques like atomic layer deposition (ALD) and selective CVD have made significant progress toward atomic-scale synthesis control. For example, Mehravar et al. employed selective CVD to deposit Ru on Ni/rGO, achieving remarkable dispersion and catalytic activity in propane steam reforming.[27] Similarly, Parnian et al. demonstrated enhanced reducibility and selectivity of Ru catalysts via selective CVD on Co/$\gamma$-$Al_2O_3$ for Fischer–Tropsch synthesis.[28]

Building on these breakthroughs, the present study introduces a dual-temperature selective CVD approach combined with real-time, in situ gaseous FTIR spectroscopy to fabricate Fe/Pd-rGO and Co/Pd-rGO catalysts. Central to this work is the introduction of a novel concept—

called the FTB—which defines precisely controlled temperature windows optimized for each metal system to govern precursor decomposition and surface reactions with ultrahigh precision. This strategy not only enables exceptional process reproducibility and material quality but also facilitates targeted nanoscale interface engineering. The integration of real-time FTIR monitoring further enhances synthetic robustness, marking a significant advance in catalytic material fabrication and setting new standards for atomic-level catalyst design.

## 2. Experimental

### 2.1 Materials

The chemicals used for catalyst synthesis were: graphite fine powder (≥99.9%, Sigma-Aldrich, USA), sulfuric acid ($H_2SO_4$, 95–97%, Sigma-Aldrich, USA), phosphoric acid ($H_3PO_4$, ≥85%, Sigma-Aldrich, USA), potassium permanganate ($KMnO_4$, ≥99%, Sigma-Aldrich, USA), hydrogen peroxide ($H_2O_2$, 35% w/w, Sigma-Aldrich, USA), palladium(II) chloride ($PdCl_2$, ≥59% Pd basis, Merck, Germany), sodium borohydride ($NaBH_4$, ≥98%, Sigma-Aldrich, USA), ferrocene ($Fe(C_5H_5)_2$, ≥98%, Sigma-Aldrich, USA), and cobaltocene ($Co(C_5H_5)_2$, ≥99%, Sigma-Aldrich, USA).

### 2.2 Samples Preparation

### 2.1 Preparation of GO

Graphite oxide was prepared using an adapted Hummers' method [29]. Initially, 45 mL of concentrated $H_2SO_4$ and 5 mL of $H_3PO_4$ were mixed at room temperature. Then, 1 g of pure graphite powder was added and stirred vigorously at 500 rpm in an ice bath. Subsequently, 6 g of $KMnO_4$ was gradually incorporated, and the mixture's temperature was slowly increased to 35 °C over 30 minutes, then maintained for 48 hours. After cooling, $H_2O_2$ was added dropwise until the solution turned yellow. The product was washed with deionized water, centrifuged multiple times, and vacuum-dried at 70 °C for 4 hours.

## 2.2 Preparation of Pd/rGO

The Concurrent Reduction method for synthesizing a Pd/rGO catalyst involves dispersing 1.0 g of GO in 200 mL of deionized water through 30-minute ultrasonication, followed by adding 0.052 g of $PdCl_2$ and stirring at 500 rpm for 1 hour. Subsequently, 100 mL of a 0.02 M $NaBH_4$ aqueous solution is added dropwise over 10 minutes to co-reduce GO and $PdCl_2$, and the mixture is incubated at 85 °C for 3 hours. The resulting catalyst is separated by centrifugation at 4,000 rpm, and vacuum-dried at 60 °C for 12 hours. Inductively coupled plasma-optical emission spectroscopy (ICP-OES) analysis confirms a palladium loading of 3.8 wt%.

### 2.3.2 Preparation of Fe on Pd/rGO

The selective Fe deposition method employs CVD to deposit Fe nanoparticles onto Pd/rGO using ferrocene as the precursor. Initially, 0.5 g of ferrocene is placed in the precursor chamber, while 1.0 g of Pd/rGO (3.8 wt% Pd) is loaded into the deposition chamber. The system is degassed at 200 °C and cooled to ambient temperature. Ferrocene sublimation is initiated by heating the precursor chamber to 80 °C under a continuous argon flow at 10 mL $min^{-1}$. Simultaneously, hydrogen is introduced to the deposition zone at 20 mL $min^{-1}$ to facilitate reduction.The deposition zone temperature is incrementally raised from 30 °C to 400 °C in 10 °C steps, with CVD conducted at each interval to achieve controlled Fe deposition. Real-time gas-phase FTIR spectroscopy monitors the process, optimizing conditions for selective Fe nanoparticle formation on Pd active sites.

### 2.3.2 Preparition of Co on Pd/rGO

The selective cobalt deposition method harnesses CVD to intricately anchor cobalt nanoparticles onto Pd/rGO, using cobaltocene as the precursor. A 0.5 g portion of cobaltocene is loaded into the precursor chamber, paired with 1.0 g of Pd/rGO (3.8 wt% Pd) in the deposition chamber. After degassing at 200 °C and cooling to room temperature, the precursor

chamber is gently heated to 85 °C under a steady argon stream flowing at 10 mL $min^{-1}$ to trigger sublimation, while hydrogen gas, flowing at 20 mL $min^{-1}$, is directed into the deposition zone to facilitate reduction. The deposition zone temperature is methodically ramped from 30 °C to 400 °C in 10 °C increments, with CVD executed at each step to sculpt precise cobalt nanoparticle formation. Real-time gas-phase FTIR spectroscopy vigilantly tracks the process, ensuring optimal conditions for selective cobalt integration onto Pd active sites, delivering a finely tuned catalyst.

### 2.4 Characterization Techniques

FTIR spectroscopy was performed using a Nicolet iS50 spectrometer (Thermo Fisher Scientific, USA) to analyze effluent gases from the CVD reaction, covering a wavenumber range of 400–4000 $cm^{-1}$. X-ray diffraction (XRD) analysis was conducted on a Rigaku SmartLab diffractometer (Rigaku, Japan) using Cu $K\alpha$ radiation ($\lambda$ = 1.5406 Å), with diffraction patterns collected over a $2\theta$ range of 10–85° at a scan rate of 2° $min^{-1}$ to determine the phase composition, crystallinity, and lattice parameters of Pd/rGO nanomaterials. The concentrations of Pd, Co and Fe in the catalysts were quantified via ICP-OES using an Agilent 5110 instrument (Agilent Technologies, USA), providing precise metal loading measurements.

## 3. Results and Discussion

### 3.1 charactrization of Pd/rGO

The FTIR spectrum of Pd-rGO, as depicted in Figure 1(a), elucidates the surface chemistry of this catalytically active material. A prominent broad band at ~3400 $cm^{-1}$, attributed to O–H stretching vibrations, indicates the presence of hydroxide groups or adsorbed water, consistent with residual hydration on the rGO surface. [30] Peaks at ~2920 and ~2800 $cm^{-1}$, assigned to C–H stretching, and a peak at 1384 $cm^{-1}$, linked to C–H bending, reveal residual hydrocarbon functionalities at defect sites or edges. [19], [31] A sharp peak at 1620 $cm^{-1}$ confirms the

restoration of conjugated C=C bonds, characteristic of the $sp^2$-hybridized carbon lattice in rGO.[19] Additionally, a band at ~1110 $cm^{-1}$ corresponds to C–O stretching, reflecting persistent oxygen-containing groups. [19] These spectral features collectively affirm Pd-rGO as a partially reduced, functionalized graphene material with enhanced surface reactivity for catalytic applications.

The XRD pattern of the Pd/ rGO sample shows peaks at $2\theta$ values of 24.8°, 39°, 42.8°, 45°, 66°, and 79°, elucidating its crystallographic structure (Figure 1(b)). The peak at 24.8° corresponds to the (002) plane of rGO, reflecting its graphitic layered structure, while the peaks at 39°, 45°, 66°, and 79° match the (111), (200), (220), and (311) planes of face-centered cubic (FCC) Pd, respectively, per JCPDS 46-1043, confirming crystalline Pd nanoparticles. The peak at 42.8°, attributed to the C(100) plane, indicates in-plane graphitic ordering within the rGO framework. Application of the Scherrer equation to the Pd peaks estimates the average Pd nanoparticle size to be 9.37 nm, suggesting well-dispersed, nanoscale Pd crystallites on the rGO support. This composite material exhibits no significant impurity phases, with the XRD pattern affirming the structural integrity of both Pd and rGO components.

**Figure 1**

### 3.2 Selective CVD of Fe on Pd/rGO

The Gas-FTIR analysis of ferrocene decomposition on Pd/rGO (3.8 wt% Pd) during CVD provides insight into the temperature-dependent catalytic pathways involved. At the sublimation temperature of approximately 80 °C, ferrocene's vapor pressure (~94 Pa)[32] facilitates efficient precursor delivery to the reaction zone, where hydrogen acts to cleave ligands and promote hydrogenation reactions. FTIR spectra collected across a temperature range of 30 to 400 °C (Figure 2(a)) reveal characteristic vibrational modes. Persistent peaks between 550–750 $cm^{-1}$ correspond to out-of-plane C–H bending and ring deformation modes associated with cyclopentadienyl ($C_5H_5$), cyclopentadiene ($C_5H_6$), and cyclopentene ($C_5H_8$).

The 750–1000 $cm^{-1}$ region features in-plane C–H bending vibrations, while the 1250–1800 $cm^{-1}$ and 3400–4000 $cm^{-1}$ regions indicate the presence of water ($H_2O$). Additional peaks at 2080–2220 $cm^{-1}$ are attributed to C≡O stretching in CO, whereas signals between 2250–2500 $cm^{-1}$ correspond to C=O stretching in $CO_2$. The broad 2700–3200 $cm^{-1}$ region encompasses C–H stretching modes from $C_5H_6$, $C_5H_8$, and methane ($CH_4$). Control experiments without ferrocene (Figure 2(b)) demonstrate that $H_2O$ and $CO_2$ peaks are background features originating from residual moisture or ambient air, remaining stable across the temperature interval.

In the lower temperature range (<100 °C), the prominent 550–750 $cm^{-1}$ peak predominantly signifies the sublimation of intact ferrocene or its derivatives ($Fe(C_5H_5)_2$). As the temperature increases from 100 °C to 240 °C, the emergence of peaks within 750–1000 $cm^{-1}$ and the intensification of C–H stretching signals at 2884 and 2966 $cm^{-1}$—both amplifying with rising temperature—serve as clear evidence of catalyzed ferrocene decomposition. These spectral changes correspond to $H_2$-assisted ligand cleavage, resulting in the liberation of metallic Fe and the formation of unsaturated hydrocarbons such as $C_5H_6$ and $C_5H_8$. Above 240 °C, the FTIR spectra indicate a decline in $C_5H_6$- and $C_5H_8$-related signals, while peaks associated with $CH_4$ at ~3100 $cm^{-1}$ (Figure 2 (c)) and CO at 2080–2220 $cm^{-1}$ increase in intensity. This shift suggests further hydrocarbon cracking and ring-opening reactions leading to $CH_4$ formation, along with partial oxidation where oxygen functionalities on rGO (as shown in Figure 1(a)) react with evolved carbon species to produce CO. The persistent 550–750 $cm^{-1}$ band confirms the presence of residual aromatic ring fragments. The progressive rise in CO signals reflects activation of oxygen-containing groups on rGO at elevated temperatures, highlighting their role in oxidation pathways. Overall, these observations emphasize the catalytic influence of Pd/rGO in directing ferrocene decomposition toward specific gaseous byproducts, with temperature serving as a critical parameter for optimizing Fe deposition processes. The thermal

decomposition of ferrocene on rGO produces $C_5H_6$, $C_5H_8$, and $CH_4$, consistent with our previous observations of nickelocene ($Ni(C_5H_5)_2$) decomposition on boron nitride, which were validated by gas chromatography. [33]

**Figure 2**

The thermal behavior of ferrocene decomposition during CVD on rGO was thoroughly examined to elucidate its influence on Fe deposition processes. FTIR spectra, shown in Figure 3, reveal vibrational modes analogous to those observed on Pd/rGO, including a persistent peak in the 550–750 $cm^{-1}$ range attributable to out-of-plane C–H bending and ring deformation within $C_5H_5$, $C_5H_6$, $C_5H_8$ groups. Additionally, bands at 750–1000 $cm^{-1}$ correspond to in-plane C–H bending modes of unsaturated hydrocarbons, while signals at 2080–2220 $cm^{-1}$ are characteristic of CO stretching, and 2250–2500 $cm^{-1}$ are associated with $CO_2$ vibrational modes. The broad region of 2700–3200 $cm^{-1}$ encompasses C–H stretching vibrations.

A notable difference compared to Pd/rGO is the absence of the prominent peaks at 2884 and 2966 $cm^{-1}$—assigned to symmetric and asymmetric C–H stretches of $C_5H_8$'s $CH_2$ groups and $C_5H_6$'s $CH_2$—above 200 °C, indicating less formation of unsaturated hydrocarbons in the rGO system. Instead, a pronounced $CH_4$ peak appears near 3100 $cm^{-1}$ at temperatures exceeding 290 °C, suggesting that the decomposition pathway on rGO favors hydrocarbon cracking leading to $CH_4$ rather than the accumulation of $C_5H_6$ and $C_5H_8$.

**Figure 3**

A comparative analysis of Fe CVD on Pd/rGO versus bare rGO was performed by integrating the peak areas of characteristic gas-phase products obtained from FTIR spectra over a wide temperature range. This quantitative approach enables identification of temperature-dependent catalytic activity and mechanistic distinctions, revealing the concept of a FTB, a temperature boundary marking the transition between distinct decomposition regimes. The temperature-

dependent integrated absorbance areas of hydrocarbon intermediate bands (C–H stretching modes, 2700–3200 $cm^{-1}$) were quantitatively compared between both systems (Figure 4).

This analysis reveals markedly enhanced ferrocene decomposition on Pd/rGO relative to bare rGO, particularly within the critical FTBs range (100–270 °C) – the optimal temperature window for efficient Fe deposition. This enhanced decomposition on Pd/rGO correlates with the high intensity of the 2884/2966 $cm^{-1}$ peaks, reflective of active formation of $C_5H_6$ and $C_5H_8$. These findings highlight Pd's superior catalytic capability to dissociate $H_2$ and facilitate hydrogenation reactions, promoting ligand removal and hydrocarbon formation. Conversely, rGO alone exhibits sluggish decomposition behavior attributable to its limited catalytic activity, primarily driven by surface defects and oxygen functionalities. In this system, hydrocarbon cracking predominantly results in $CH_4$ formation at higher temperatures, indicating a shift toward $C_5H_6$ fragmentation pathways with minimal generation of higher unsaturated hydrocarbons.

**Figure 4**

### 3.3 Selective CVD of Co on Pd/rGO

The CVD of Co on Pd/rGO using cobaltocene as a precursor reveals temperature-dependent catalytic pathways that diverge significantly from those observed in ferrocene CVD. At its sublimation temperature of 85 °C, cobaltocene exhibits a vapor pressure of ~91 Pa, [32] enabling effective precursor delivery. Decomposition initiates at a low temperature of ~40 °C, driven by cobaltocene's 19-electron electronic instability and weaker Co–$C_5H_5$ bonds (~180 kJ/mol), contrasting with ferrocene's more stable decomposition profile.

Gas-phase FTIR spectroscopy reveals distinct vibrational bands (Figure 5(a)), with onset peaks detected from ~40 °C including 550–750 $cm^{-1}$ (out-of-plane C–H bending and ring deformation of $C_5H_5$), 800 $cm^{-1}$ (=CH bending modes typical of CH wagging or $CH_2$ rocking in acyclic alkenes), 1037 and 1094 $cm^{-1}$ (in-plane =CH bending/stretching consistent with

acyclic alkenes such as 1-pentene), and around 1300 $cm^{-1}$ ($CH_2$ stretching vibrations associated with linear alkanes like pentane) [34]. Weak hydrocarbon C–H stretching modes at 2884 and 2966 $cm^{-1}$ also appear starting at this temperature. The intensity of the 800, 1037, 1094, ~1300, and 2884/2966 $cm^{-1}$ bands grows up to 130 °C, after which they diminish.

Environmental background signals for $CO_2$ (2250–2500 $cm^{-1}$) and $H_2O$ (~1500–1700 and ~3500–3700 $cm^{-1}$) are present throughout (Figure 5(b)), while CO (2080–2220 $cm^{-1}$, C≡O stretching) and $CH_4$ (~3100 $cm^{-1}$) evolve at elevated temperatures. Unlike ferrocene decomposition, FTIR spectra lack peaks in the 750–1000 $cm^{-1}$ range (in-plane C–H bending in cyclic structures), indicating the absence of stable cyclic hydrocarbon intermediates.

The decomposition pathway involves rapid ligand dissociation ($Co(C_5H_5)_2 \rightarrow Co + 2\ C_5H_6$) beginning near 40 °C. The persistent 1037 and 1094 $cm^{-1}$ peaks provide clear evidence for the formation of acyclic hydrocarbons like 1-pentene ($CH_2$=CH–$CH_2$–$CH_2$–$CH_3$), while the 800 $cm^{-1}$ band confirms =CH vibrations characteristic of acyclic alkenes. The band near 1300 $cm^{-1}$ corresponds to linear alkanes such as pentane ($CH_3$–$CH_2$–$CH_2$–$CH_2$–$CH_3$), further supporting rapid ring-opening of the cyclopentadienyl ligands. The increasing intensity of hydrocarbon C–H stretching modes (2884 and 2966 $cm^{-1}$) up to 130 °C reflects accumulation of these species.

Beyond 130 °C, the progressive attenuation of the hydrocarbon C–H signals (2884/2966 $cm^{-1}$) and peaks at 800, 1037, 1094, and ~1300 $cm^{-1}$ coincides with the rise of $CH_4$ (~3100 $cm^{-1}$) and CO (2080–2220 $cm^{-1}$) bands (Figure 5(c)). This transition indicates hydrocarbon cracking to $CH_4$ and oxidation of residual carbon species by surface O–H and C–O functionalities on rGO, producing CO.

**Figure 5**

The thermal decomposition of cobaltocene during CVD on pristine rGO was investigated to delineate catalytic influences and mechanistic pathways relevant to cobalt deposition. Gas-

phase FTIR spectra collected from 30 to 400 °C reveal key vibrational signatures (Figure 6). Even prior to decomposition, peaks in the 550–750 $cm^{-1}$ range (out-of-plane C–H bending and ring deformation of $C_5H_5$) are detectable. Decomposition initiates at a higher threshold of approximately 150 °C, marked by the emergence of peaks at 800 $cm^{-1}$ (=CH bending in acyclic alkenes such as CH wag or $CH_2$ rock), 1037 and 1094 $cm^{-1}$ (in-plane =CH bending/stretching modes consistent with acyclic alkenes like 1-pentene), ~1300 $cm^{-1}$ ($CH_2$ stretching in linear alkanes like pentane), and symmetric/asymmetric C–H stretching near 2884/2966 $cm^{-1}$[34]. Notably, intensities of these peaks remain weak at decomposition onset. Absence of bands in the 750–1000 $cm^{-1}$ region confirms lack of stable cyclic hydrocarbons. Background signals corresponding to $CO_2$ (2250–2500 $cm^{-1}$) and $H_2O$ (~1500–1700 and ~3500–3700 $cm^{-1}$) are observed throughout, while $CH_4$ (3100 $cm^{-1}$) and CO (2080–2220 $cm^{-1}$) manifest at elevated temperatures.

Cobaltocene decomposition on rGO begins around 150 °C with rapid ligand dissociation, facilitated by catalytic sites associated with surface defects and oxygen-containing moieties on rGO ($Co(C_5H_5)_2 + H_2 \rightarrow Co$ + gaseous hydrocarbon products). The simultaneous presence of 1037 and 1094 $cm^{-1}$ peaks evidences the formation of acyclic hydrocarbons such as 1-pentene, while the 800 $cm^{-1}$ peak confirms =CH bending vibrations. The ~1300 $cm^{-1}$ peak denotes linear alkanes like pentane, indicating rapid ring-opening processes. The relatively low catalytic activity of rGO, compared to Pd/rGO, impedes extensive hydrogenation, resulting in comparatively weak hydrocarbon vibrational intensities.

At temperatures exceeding 230 °C, hydrocarbon C–H vibrational bands (2884/2966 $cm^{-1}$) decrease, concurrent with the onset of $CH_4$ (3100 $cm^{-1}$) and increased CO (2080–2220 $cm^{-1}$) signals. These spectral evolutions signify hydrocarbon cracking and oxidation of carbonaceous residues by rGO surface O–H and C–O groups, yielding CO. The early appearance of acyclic hydrocarbon signatures (800, 1037, 1094, ~1300 $cm^{-1}$) and C–H stretches in the 2884–2966

$cm^{-1}$ range, followed by signals in the 2700–3200 $cm^{-1}$ window, underscores the dominant formation of acyclic species such as 1-pentene and pentane during the decomposition process.

**Figure 6**

Quantitative analysis of the integrated absorbance in the C–H stretching region (2700–3200 $cm^{-1}$), plotted as a function of temperature in Figure 6, reveals clear differences between Co CVD on Pd/rGO and on rGO. On Pd/rGO, significantly higher integrated peak areas appear at lower temperatures, with onset near 40°C, indicating earlier and more efficient formation of hydrocarbon intermediates. In contrast, Co CVD on rGO exhibits substantially smaller integrated peak areas in this lower temperature range, with decomposition onset shifted to higher temperatures (150 °C) and overall reduced hydrocarbon signals.

This divergence in integrated peak areas delineates a FTB between approximately 40 and 140 °C, identifying a critical temperature window where Pd/rGO catalysis markedly accelerates cobaltocene decomposition compared to rGO alone. Above this threshold, hydrocarbon intermediates decrease on both substrates due to ring-opening reactions, $CH_4$ formation, and CO evolution; however, Pd/rGO consistently maintains higher catalytic activity throughout the temperature range.

**Figure 7**

### 3.4 Comparative Analysis of Ferrocene and Cobaltocene Decomposition on Pd/rGO and rGO Substrates

The CVD of ferrocene and cobaltocene on Pd/rGO and rGO substrates exhibits distinctly different decomposition behaviors dictated by their electronic structures and the catalytic properties of the substrates. Ferrocene, characterized by a stable 18-electron configuration and relatively strong Fe–$C_5H_5$ bonds (~230 kJ/mol), undergoes thermal decomposition at higher temperatures (~100 °C on Pd/rGO and ~270 °C on rGO). In contrast, cobaltocene, with its

electronically unstable 19-electron configuration and weaker Co–$C_5H_5$ bonds (~180 kJ/mol), decomposes at markedly lower temperatures (~40 °C on Pd/rGO and ~150 °C on rGO).

Gas-phase FTIR spectroscopy, as summarized in Table 1, indicates that ferrocene produces unsaturated cyclic hydrocarbon intermediates, while cobaltocene rapidly forms acyclic hydrocarbons, with both generating $CH_4$ at elevated temperatures. Cobaltocene's decomposition involves rapid ligand dissociation and stepwise hydrogenation, accelerating early ring-opening to yield acyclic hydrocarbons. This process is enhanced by cobalt's redox flexibility (Co(0) to Co(III)) and strong Co–Pd–rGO interactions, with hydrocarbon cracking at high temperatures leading to $CH_4$ formation. In contrast, ferrocene's electronic stability delays ring-opening, forming unsaturated cyclic intermediates with $CH_4$ produced at high temperatures through limited hydrocarbon cracking. Palladium in Pd/rGO enhances hydrogenation of cobaltocene-derived species, promoting saturated hydrocarbons and $CH_4$ production at elevated temperatures, whereas ferrocene undergoes minimal hydrogenation, preserving cyclic structures.

**Table١**

On rGO substrates, where catalysis relies on surface defects and oxygen-containing groups, both metallocenes require higher decomposition temperatures, yet cobaltocene initiates earlier. ٢The O–H and C–O groups on rGO facilitate oxidation of carbon intermediates, leading to CO and $CH_4$ production at high temperatures. Cobaltocene exhibits stronger CO signals due to its more facile decomposition kinetics, while $CH_4$ production at elevated temperatures is comparable for both metallocenes.

These findings underscore the critical roles of electronic configuration and Pd/rGO catalysis in directing metallocene decomposition pathways during CVD. Catalyzed by Pd/rGO, cobaltocene rapidly generates acyclic hydrocarbons and $CH_4$, whereas ferrocene promotes the formation of persistent unsaturated cyclic intermediates with $CH_4$ production. Importantly,

Pd's catalytic effect promotes the initial deposition of iron and cobalt nanoparticles in close proximity to Pd sites before these nanoparticles anchor onto the rGO substrate.

### 3.5 Elemental Analysis and Evidence of Selective Deposition

To provide quantitative confirmation of selective Fe and Co deposition, ICP-OES elemental analysis was conducted. The results are summarized in Table 2.

**Table 2**

The ICP results clearly demonstrate that Fe and Co preferentially deposit on Pd-decorated rGO, with loadings significantly higher than those on bare rGO. The small amounts detected on rGO (3.0 wt% Fe and 4.2 wt% Co) originate from non-selective thermal decomposition of precursors at elevated temperatures outside the FTB window, where precursor breakdown occurs in the absence of catalytic activation. Within the FTB regime, deposition on rGO is negligible, consistent with the in-situ Gas-FTIR observations.

In contrast, Pd nanoparticles act as highly efficient catalytic centers that significantly lower the decomposition onset temperatures of ferrocene (~100 °C) and cobaltocene (~40 °C). This catalytic activation accelerates precursor decomposition and promotes direct anchoring of Fe and Co species onto Pd sites. The much higher loadings observed for Pd/rGO (22.0 wt% Fe and 27.5 wt% Co) therefore reflect the synergistic effect of Pd in hydrogen dissociation and ligand removal, processes that facilitate rapid decomposition kinetics and selective metal–Pd interactions.

From a mechanistic and electronic perspective, Pd's metallic nature and high electron density play a pivotal role in facilitating charge transfer processes at the Pd–metal–rGO interface. Pd acts as an electron reservoir, donating electron density to Fe and Co atoms, which stabilizes these species via d-band interactions and partial covalent bonding, thereby strengthening metal-metal and metal-support interactions. Additionally, the high electrical conductivity of rGO enables efficient charge delocalization, reinforcing this electronic coupling and enhancing catalytic activity.

The electronic interplay at this triple interface lowers the activation energy for precursor decomposition by weakening metal–ligand bonds through back-donation of electron density from Pd to antibonding

orbitals of the ligands. This effect not only accelerates ligand removal but also stabilizes intermediate metal species, promoting selective nucleation and growth on Pd sites rather than on the rGO surface alone.

Together with Gas-FTIR evidence, the ICP data provide robust quantitative proof of selective deposition. These results not only support the mechanistic interpretation based on the FTB concept but also highlight the crucial role of Pd nanoparticles in enabling efficient, selective metal incorporation, whereas bare rGO only exhibits minor, non-selective deposition under high-temperature conditions.

### 3.6. Comparative perspective on selective CVD methodologies

To further contextualize the present findings, Table 3 provides a comparative summary of representative studies on selective CVD and atomic-scale interface engineering. Early advances in site-selective ALD, such as the seminal work of Kim et al. [35] on Pt nucleation at graphene line defects, demonstrated that atomic-scale structural inhomogeneities can act as highly specific nucleation centers. Subsequent developments, including area-selective ALD/CVD strategies summarized by Parsons and Clark [36], have systematically catalogued how surface chemistry, inhibitor layers, and adsorption energetics dictate spatial control. Grillo et al. [37] extended this to temperature- and chemistry-dependent selectivity for Ru deposition on patterned oxides, highlighting the importance of thermal windows analogous to the FTB concept employed in the present study.

Sequential selective CVD, as demonstrated in our earlier work on Ru–Ni/rGO, provided direct evidence that engineered bimetallic interfaces not only can be constructed with high selectivity but also deliver superior catalytic performance, particularly in propane steam reforming [27]. More recent studies, such as the site-specific CVD growth on 3D nanoarchitectures (Porrati et al. [38]) and beam-assisted maskless selective CVD [39], expand the scope of spatially resolved deposition to complex geometries and localized activation modes.

In this context, the Gas-FTIR–guided selective CVD strategy introduced here occupies a distinctive methodological niche. By directly identifying decomposition kinetics and defining the FTB regime in situ, this approach circumvents the need for complex chemistries or patterning steps, yet still enables

selective nucleation on Pd sites with quantitative confirmation by ICP analysis. The combination of accessibility, mechanistic clarity, and compatibility with bimetallic interface formation distinguishes the present methodology from existing approaches and positions it as a practical route for engineering catalytically relevant heterostructures.

**Table 3**

## 4. Conclusion

This study establishes the *Frontier Thermal Bulwark* concept as a robust mechanistic and methodological framework for selective metallocene CVD on Pd-decorated reduced graphene oxide. By delineating precise temperature windows, we demonstrate how FTB-guided control enables earlier, more efficient, and highly selective decomposition of ferrocene (~100 °C) and cobaltocene (~40 °C) on Pd/rGO compared with bare rGO. Gas-phase FTIR monitoring revealed that Pd catalysis not only facilitates $H_2$ dissociation and selective ligand removal but also directs the formation of well-defined Fe–Pd and Co–Pd interfaces, which are anticipated to enhance catalytic synergy while minimizing precious metal utilization.

Beyond confirming the distinct decomposition pathways of ferrocene and cobaltocene—cyclic intermediates versus rapid acyclic hydrocarbon formation—this work validates Pd/rGO as an effective platform for engineering nanoscale interfacial architectures. Importantly, the insights gained here extend beyond the studied systems: the FTB-guided strategy provides a generalizable approach applicable to other metallocene precursors and substrate materials, enabling systematic exploration of selective interface formation.

Looking forward, coupling ICP and Gas-FTIR with advanced operando and high-resolution techniques such as HR-TEM and XPS will allow direct atomic-scale visualization of selective interfaces and their dynamic evolution under reaction conditions. Furthermore, the structurally well-defined Fe–Pd and Co–Pd interfaces developed in this work offer promising opportunities for catalytic applications in hydrogenation, reforming, and electrocatalysis. By translating structural selectivity into functional

performance, these directions will advance the design of cost-effective, high-performance catalysts for energy and environmental technologies.

In summary, the present contribution not only introduces a validated and accessible strategy for controlled nanocatalyst synthesis but also outlines clear research trajectories, situating the work as a foundation for future advances in selective CVD and catalytic interface engineering.

**Acknowledgements**

The authors gratefully acknowledge the Catalysis and Nanostructured Materials Research Laboratory at the School of Chemical Engineering, University of Tehran, for providing essential facilities and resources. We also thank the Iran National Science Foundation (INSF) for their support under Grant No. 4026894.

## 5. References

[1] J. Liu, L. wang, F. Okejiri, *et al.*, "Deep Understanding of Strong Metal Interface Confinement: A Journey of Pd/FeO x Catalysts," *ACS Catal.*, vol. 10, no. 15, pp. 8950–8959, Aug. 2020, doi: 10.1021/acscatal.0c01447.

[2] D. W. Elliott and W. Zhang, "Field Assessment of Nanoscale Bimetallic Particles for Groundwater Treatment," *Environ. Sci. Technol.*, vol. 35, no. 24, pp. 4922–4926, Dec. 2001, doi: 10.1021/es0108584.

[3] Y. Hong, H. Zhang, J, Sun, *et al.*, "Synergistic Catalysis between Pd and Fe in Gas Phase Hydrodeoxygenation of m -Cresol," *ACS Catal.*, vol. 4, no. 10, pp. 3335–3345, Oct. 2014, doi: 10.1021/cs500578g.

[4] X. Wang, J, Li, J. Xing, *et al.*, "Novel synergistically effects of palladium-iron bimetal and manganese carbonate carrier for catalytic oxidation of formaldehyde at room temperature," *J. Colloid Interface Sci.*, vol. 656, pp. 104–115, Feb. 2024, doi: 10.1016/j.jcis.2023.11.095.

[5] R. Wojcieszak, M. N. Ghazzal, E. M. Gaigneaux, *et al.*, "Low temperature oxidation of methanol to methyl formate over Pd nanoparticles supported on γ-Fe2O3," *Catal. Sci. Technol.*, vol. 4,

no. 3, p. 738, 2014, doi: 10.1039/c3cy00859b.

[6] W. Jiang, B. Xu, Z. Xiang, *et al.*, "Preparation and reactivity of UV light-reduced Pd/α-Fe2O3 catalyst towards the hydrogenation of o-chloronitrobenzene," *Appl. Catal. A Gen.*, vol. 520, pp. 65–72, Jun. 2016, doi: 10.1016/j.apcata.2016.04.007.

[7] P. R. Ellis, C.M. Brown, P.T. Bishop, *et al.*, "High-selectivity palladium catalysts for the partial hydrogenation of alkynes by gas-phase cluster deposition onto oxide powders," *Catal. Struct. React.*, vol. 4, no. 2, pp. 1–8, Apr. 2018, doi: 10.1080/2055074X.2018.1477315.

[8] Ö. Metin, A. Mendoza-Garcia, D. Dalmızrak, *et al.*, "FePd alloy nanoparticles assembled on reduced graphene oxide as a catalyst for selective transfer hydrogenation of nitroarenes to anilines using ammonia borane as a hydrogen source," *Catal. Sci. Technol.*, vol. 6, no. 15, pp. 6137–6143, 2016, doi: 10.1039/C6CY00118A.

[9] M. Minnermann, S. Pokhrel, K. Thiel, *et al.*, "Role of Palladium in Iron Based Fischer−Tropsch Catalysts Prepared by Flame Spray Pyrolysis," *J. Phys. Chem. C*, vol. 115, no. 4, pp. 1302–1310, Feb. 2011, doi: 10.1021/jp106860d.

[10] N. Osakoo, R. Henkel, S. Loiha, *et al.*, "Palladium-promoted cobalt catalysts supported on silica prepared by impregnation and reverse micelle for Fischer–Tropsch synthesis," *Appl. Catal. A Gen.*, vol. 464–465, pp. 269–280, Aug. 2013, doi: 10.1016/j.apcata.2013.06.008.

[11] Y. Liu, L. Chen, S. Liu, *et al.*, "Role of iron-based catalysts in reducing NO emissions from coal combustion," *Chinese J. Chem. Eng.*, vol. 59, pp. 1–8, Jul. 2023, doi: 10.1016/j.cjche.2022.11.017.

[12] W. Yang, J. Ren. H. Zhang, *et al.*, "Single-atom iron as a promising low-temperature catalyst for selective catalytic reduction of NO with NH3: A theoretical prediction," *Fuel*, vol. 302, p. 121041, Oct. 2021, doi: 10.1016/j.fuel.2021.121041.

[13] T. T. Nguyen, V. H. Nguyen, R. K. Deivasigamani, *et al.*, "Facile synthesis of cobalt oxide/reduced graphene oxide composites for electrochemical capacitor and sensor

applications," *Solid State Sci.*, vol. 53, pp. 71–77, Mar. 2016, doi: 10.1016/j.solidstatesciences.2016.01.006.

[14] W. Lin, D. Smilowicz, M.A. Joaqui, *et al.*, "Controlling the Redox Chemistry of Cobalt Radiopharmaceuticals," *Angew. Chemie Int. Ed.*, vol. 63, no. 50, Dec. 2024, doi: 10.1002/anie.202412357.

[15] A. J. R. Hensley, Y. Hong, R.Zhang, *et al.*, "Enhanced Fe 2 O 3 Reducibility via Surface Modification with Pd: Characterizing the Synergy within Pd/Fe Catalysts for Hydrodeoxygenation Reactions," *ACS Catal.*, vol. 4, no. 10, pp. 3381–3392, Oct. 2014, doi: 10.1021/cs500565e.

[16] E. Yuan, C. Wang, C. Wu, *et al.*, "Constructing a Pd–Co Interface to Tailor a d-Band Center for Highly Efficient Hydroconversion of Furfural over Cobalt Oxide-Supported Pd Catalysts," *ACS Appl. Mater. Interfaces*, vol. 15, no. 37, pp. 43845–43858, Sep. 2023, doi: 10.1021/acsami.3c09234.

[17] A. Shukla, R. K. Singha, T. Sasaki, *et al.*, "Synthesis of Highly Active Pd Nanoparticles Supported Iron Oxide Catalyst for Selective Hydrogenation and Cross-Coupling Reactions in Aqueous Medium," *ChemistrySelect*, vol. 4, no. 17, pp. 5019–5032, May 2019, doi: 10.1002/slct.201900358.

[18] S. Sahil and N. Gupta, "Nanoarchitectonics of Palladium Nanoparticles Supported on Carbon-Based Heterogeneous Catalysts for C─H Activation Reaction," *ChemCatChem*, vol. 17, no. 9, May 2025, doi: 10.1002/cctc.202401840.

[19] S. Mehravar, S. Fatemi, and M. Komiyama, "The role of cerium intercalation in the efficient dry exfoliation of graphene layers at a low temperature," *Diam. Relat. Mater.*, vol. 101, p. 107615, Jan. 2020, doi: 10.1016/j.diamond.2019.107615.

[20] S. F. Adil, M. Ashraf, M. Mujeep Khan, *et al.*, "Advances in Graphene/Inorganic Nanoparticle Composites for Catalytic Applications," *Chem. Rec.*, vol. 22, no. 7, Jul. 2022, doi:

10.1002/tcr.202100274.

[21] M. Formenti, M. Pagliaro, C. Della Pina, *et al.*, "Graphene oxide in palladium nanoparticle (GrafeoPlad): a new class of catalytic materials for heterogeneous catalysis," Apr. 18, 2023. doi: 10.26434/chemrxiv-2023-hw1tj.

[22] R. Xie, F. Qin, L. Zhou, *et al.*, "Supported palladium nanocubes reduced by graphene oxide and surface-cleaned for enhanced electrocatalytic activity," *J. Alloys Compd.*, vol. 994, p. 174697, Aug. 2024, doi: 10.1016/j.jallcom.2024.174697.

[23] V. Kishnani, A. Yadav, K. Mondal, *et al.*, "Palladium-Functionalized Graphene for Hydrogen Sensing Performance: Theoretical Studies," *Energies*, vol. 14, no. 18, p. 5738, Sep. 2021, doi: 10.3390/en14185738.

[24] N. Li, S. Tang, and X. Meng, "Reduced Graphene Oxide Supported Bimetallic Cobalt–Palladium Nanoparticles with High Catalytic Activity towards Formic Acid Electro-oxidation," *J. Mater. Sci. Technol.*, vol. 31, no. 1, pp. 30–36, Jan. 2015, doi: 10.1016/j.jmst.2014.09.007.

[25] O. F. Aldosari, "Iron-palladium supported graphene as an efficient bimetallic catalyst for the selective oxidation of benzyl alcohol to benzaldehyde," *J. Saudi Chem. Soc.*, vol. 27, no. 4, p. 101671, Jul. 2023, doi: 10.1016/j.jscs.2023.101671.

[26] S. Sharma, A. Anjani, M. Kouser, *et al.*, "Palladium nanoparticles loaded over sheet-like N-doped graphene oxide: investigation of its catalytic potential in Suzuki coupling, in reduction of nitroarenes and in photodegradation of methyl orange," *New J. Chem.*, vol. 47, no. 34, pp. 16030–16042, 2023, doi: 10.1039/D3NJ02020G.

[27] S. Mehravar, S. Fatemi, and M. Komiyama, "Highly selective hydrogen production from propane by <scp>Ru–Ni</scp> core–shell nanocatalyst deposited on reduced graphene oxide by sequential chemical vapor deposition," *Int. J. Energy Res.*, vol. 44, no. 10, pp. 8000–8013, Aug. 2020, doi: 10.1002/er.5541.

[28] M. J. Parnian, A. Taheri Najafabadi, Y. Mortazavi, *et al.*, "Ru promoted cobalt catalyst on γ-

Al2O3: Influence of different catalyst preparation method and Ru loadings on Fischer–Tropsch reaction and kinetics," *Appl. Surf. Sci.*, vol. 313, pp. 183–195, Sep. 2014, doi: 10.1016/j.apsusc.2014.05.183.

[29] W. S. Hummers and R. E. Offeman, "Preparation of Graphitic Oxide," *J. Am. Chem. Soc.*, vol. 80, no. 6, pp. 1339–1339, Mar. 1958, doi: 10.1021/ja01539a017.

[30] M. Mermoux, Y. Chabre, and A. Rousseau, "FTIR and 13C NMR study of graphite oxide," *Carbon N. Y.*, vol. 29, no. 3, pp. 469–474, 1991, doi: 10.1016/0008-6223(91)90216-6.

[31] P. Divya and S. Ramaprabhu, "Platinum–graphene hybrid nanostructure as anode and cathode electrocatalysts in proton exchange membrane fuel cells," *J. Mater. Chem. A*, vol. 2, no. 14, pp. 4912–4918, 2014, doi: 10.1039/C3TA15181F.

[32] M. T. Vieyra-Eusebio and A. Rojas, "Vapor Pressures and Sublimation Enthalpies of Nickelocene and Cobaltocene Measured by Thermogravimetry," *J. Chem. Eng. Data*, vol. 56, no. 12, pp. 5008–5018, Dec. 2011, doi: 10.1021/je200815v.

[33] S. Mehravar, B. M. Garmejani, and S. Fatemi, "Nickel-deposited hexagonal boron nitride composites synthesized via chemical vapor deposition: unlocking enhanced magnetic properties for advanced technologies," *J. Mater. Chem. C*, vol. 13, no. 13, pp. 6823–6830, 2025, doi: 10.1039/D4TC05281A.

[34] W. Yang, H. Shao, L. Zou, *et al.*, "Research on Condensable Particulate Matter Emission Characteristics from Sewage Sludge Combustion," *Water, Air, Soil Pollut.*, vol. 234, no. 6, p. 372, Jun. 2023, doi: 10.1007/s11270-023-06379-5.

[35] K. Kim, H. Lee, R. W. Johnson, *et al.*, "Selective metal deposition at graphene line defects by atomic layer deposition," *Nat. Commun.*, vol. 5, no. 1, p. 4781, Sep. 2014, doi: 10.1038/ncomms5781.

[36] G. N. Parsons and R. D. Clark, "Area-Selective Deposition: Fundamentals, Applications, and Future Outlook," *Chem. Mater.*, vol. 32, no. 12, pp. 4920–4953, Jun. 2020, doi:

10.1021/acs.chemmater.0c00722.

[37] F. Grillo, J. Soethoudt, e. A. Marques, *et al.*, "Area-Selective Deposition of Ruthenium by Area-Dependent Surface Diffusion," *Chem. Mater.*, vol. 32, no. 22, pp. 9560–9572, Nov. 2020, doi: 10.1021/acs.chemmater.0c02588.

[38] F. Porrati, S. Barth, G.C. Gazzadi, *et al.*, "Site-Selective Chemical Vapor Deposition on Direct-Write 3D Nanoarchitectures," *ACS Nano*, vol. 17, no. 5, pp. 4704–4715, Mar. 2023, doi: 10.1021/acsnano.2c10968.

[39] A. Tsarapkin, K. Maćkosz, C. S. Jureddy, *et al.*, "Area-Selective Chemical Vapor Deposition of Gold by Electron Beam Seeding," *Adv. Mater.*, vol. 36, no. 23, Jun. 2024, doi: 10.1002/adma.202313571.

## Biographies

**Dr. Samira Mehravar**, a leading expert in nanotechnology and chemical engineering, holds a Ph.D. from the University of Tehran, specializing in catalysis and nanomaterials. Having completed her postdoctoral research by September 2025, she pioneered bimetallic nanocatalyst synthesis via chemical vapor deposition (CVD) for methane reforming, supported by the Iran National Science Foundation (INSF) Grant No. 4020825. With publications in ACS Catalysis and a patented nickel-boron nitride technology, Dr. Mehravar excels in electrocatalysis, photochemistry, and sustainable energy, supervising M.Sc. theses and driving innovations in clean fuel technologies at the University of Tehran.

**Prof. Abbas Ali Khodadadi**, a distinguished chemical engineering professor at the University of Tehran, is a global leader in catalysis and nanomaterials, with over 7,671 citations. His pioneering work on nanostructured catalysts and gas sensors has advanced hydrogen production and environmental monitoring, leading the Catalysis and Nanostructured Materials Research Center. Prof. Khodadadi's innovative metal oxide nanocomposites, featured in top-tier journals, cement his reputation as a trailblazer in sustainable industrial processes.

**Prof. Shohreh Fatemi**, a preeminent chemical engineering professor at the University of Tehran, heads the Adsorption, Modeling, and Nanomaterials Research Center, with over 4,377 citations. Her groundbreaking research on nanocatalysts for hydrogen production and CO2 separation using metal-organic frameworks (MOFs) is backed by INSF grants. A mentor to Ph.D. and postdoctoral scholars, including Dr. Mehravar, Prof. Fatemi's expertise in bimetallic systems drives transformative nanotechnology solutions for environmental sustainability.

**Prof. Yadollah Mortazavi**, a renowned chemical engineering professor at the University of Tehran, specializes in nanocatalysis and process engineering, with over 7,560 citations. His cutting-edge research on methane reforming and oxidative dehydrogenation catalysts shapes atomic-scale interface engineering, published in leading journals. As a key figure in the Catalysis and Nanostructured Materials Research Center, Prof. Mortazavi's innovations in nanomaterial synthesis for energy applications position him as a pivotal contributor to global sustainable technology.

## List of figures

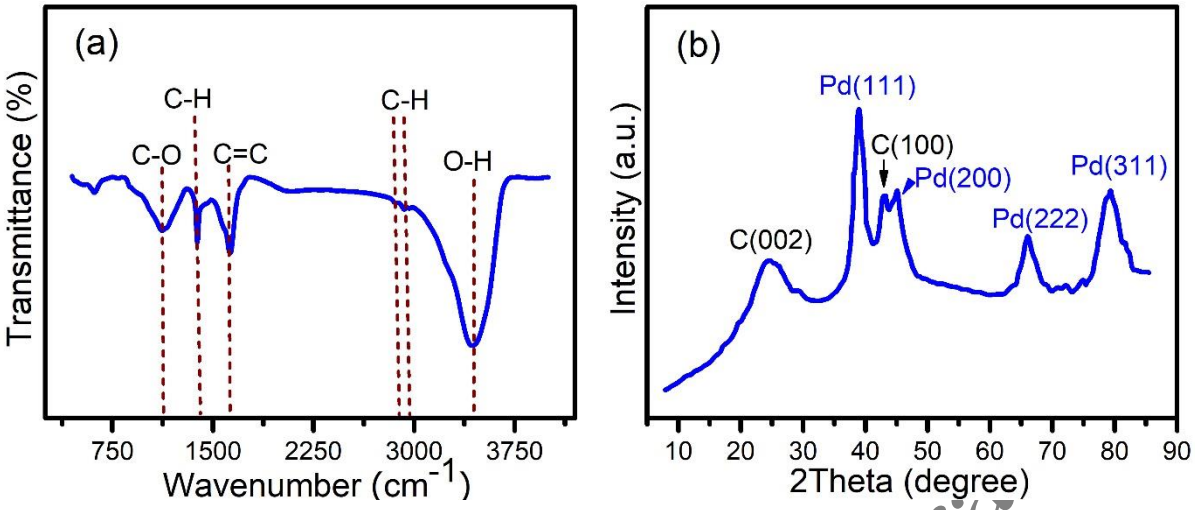


**Figure 1**

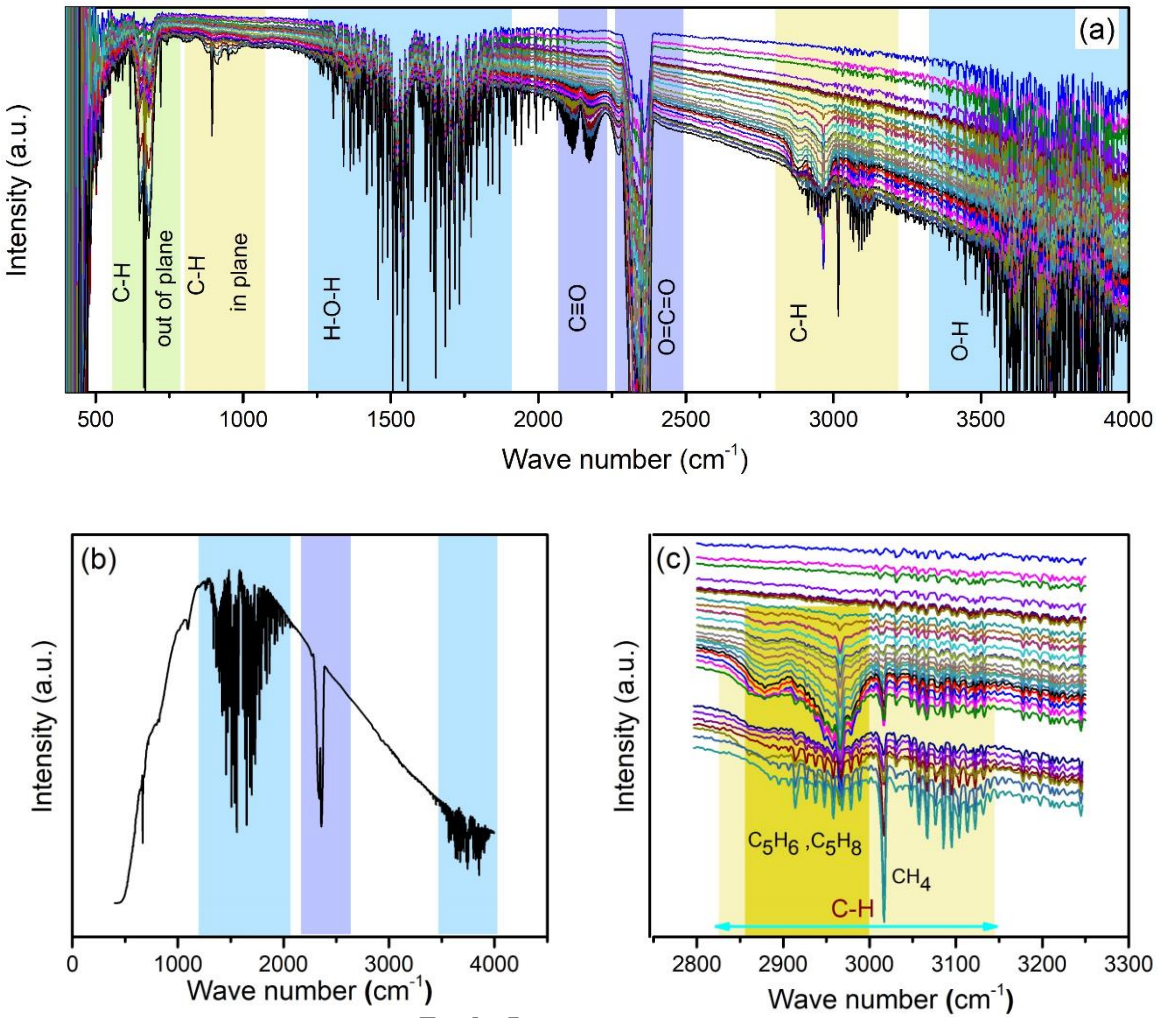


**Figure 2**

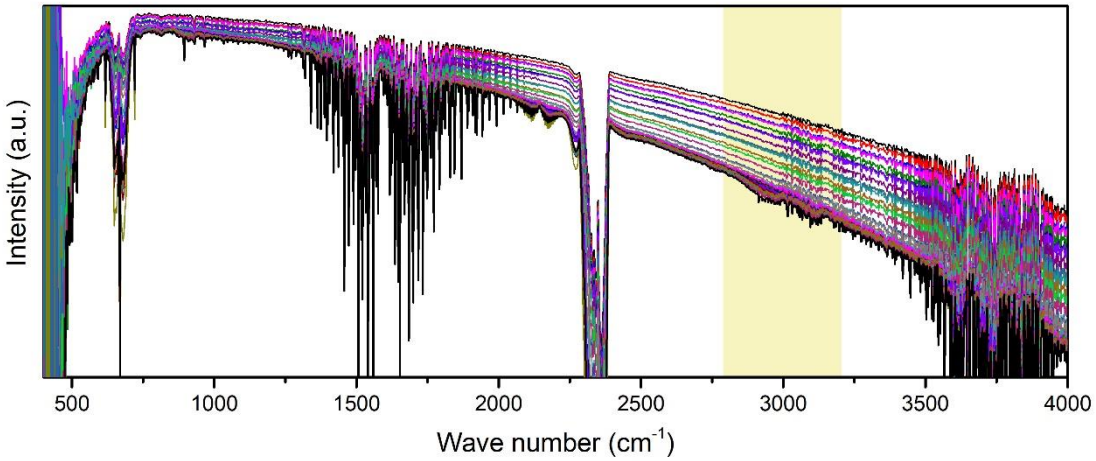


**Figure 3**

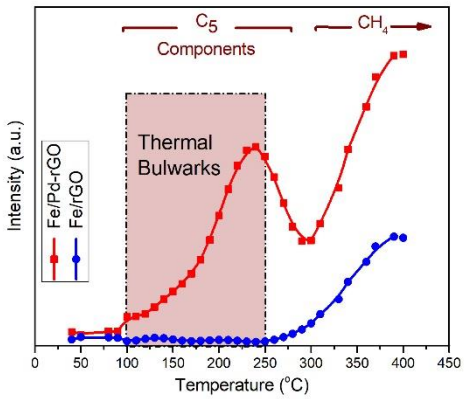


**Figure4**

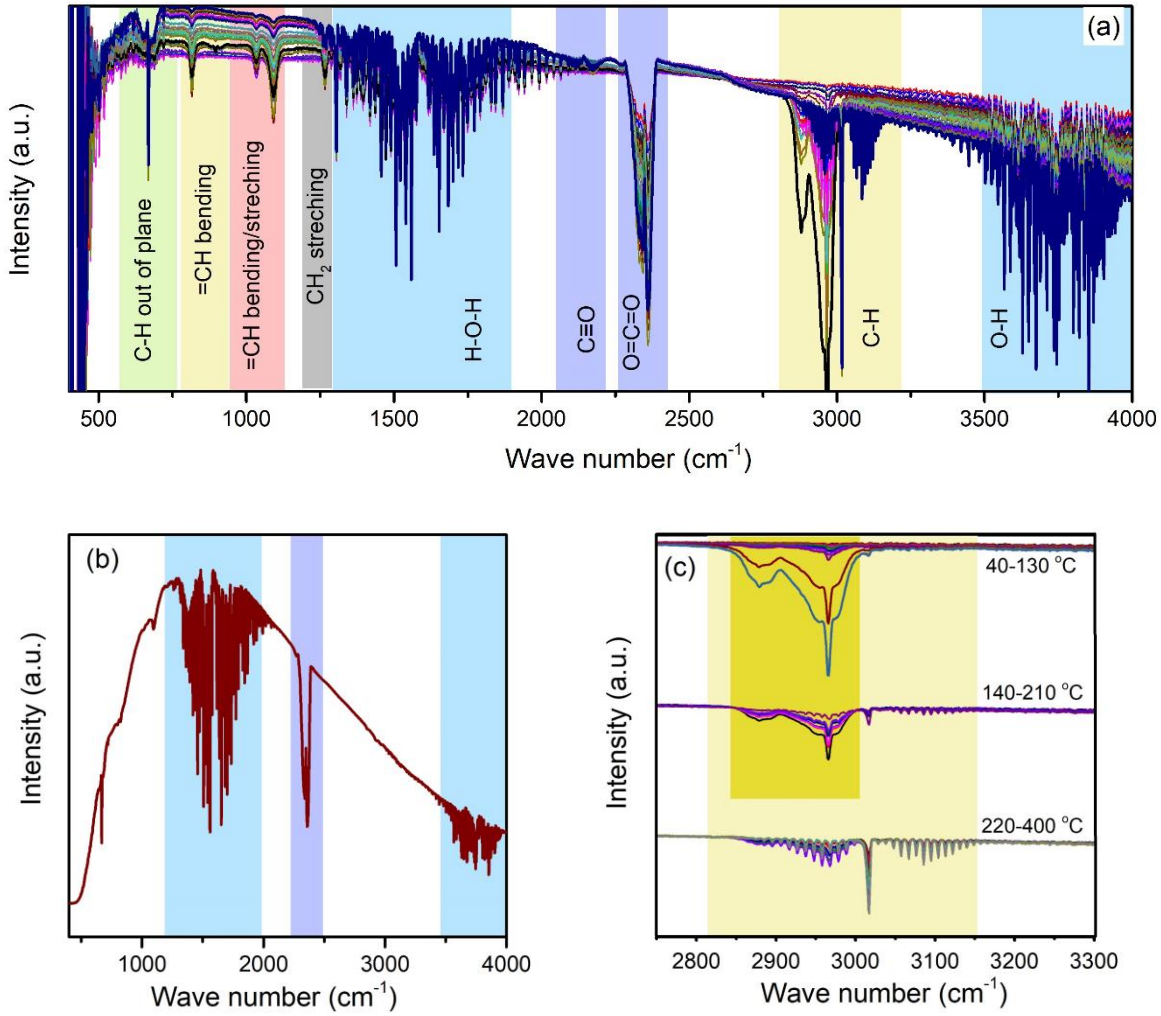


**Figure 5**

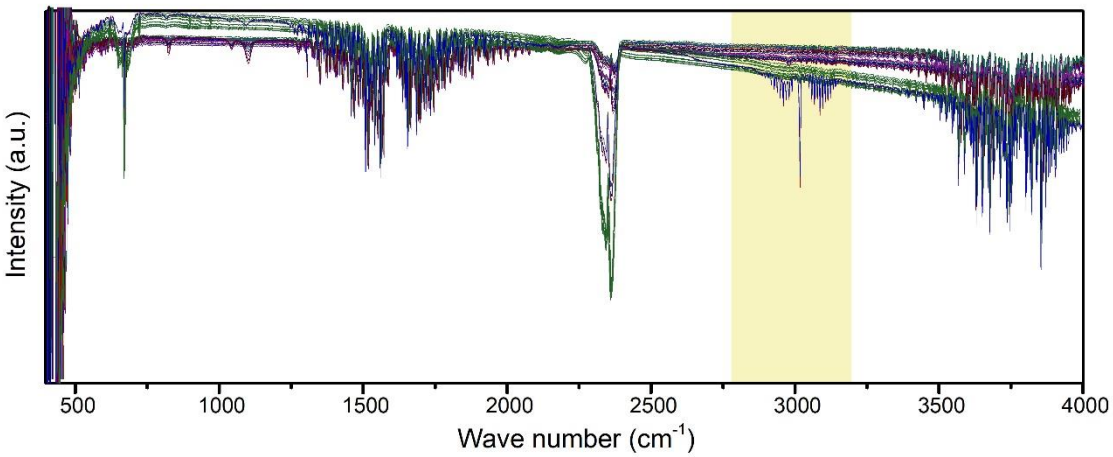


**Figure 6**

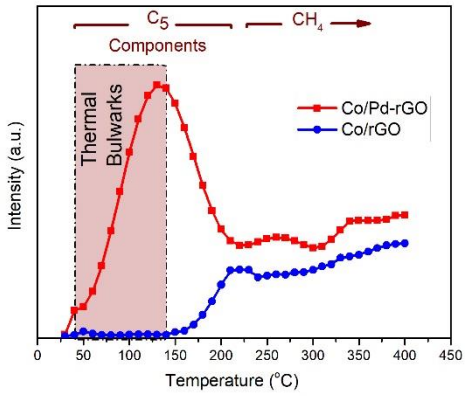


**Figure 7**

## List of Tables

## Table 1

| Parameter | Ferrocene ($Fe(C_5H_5)_2$) | Cobaltocene ($Co(C_5H_5)_2$) |
|---|---|---|
| **Decomposition Temperature** | ~100 °C (Pd/rGO), ~270 °C (rGO) | ~40 °C (Pd/rGO), ~150 °C (rGO) |
| **Ring-Opening Mechanism** | Slower; cyclic intermediates persist until >240 °C (Pd/rGO) or >270 °C (rGO) | Rapid; early formation of acyclic hydrocarbons at decomposition onset |
| **Key FTIR Bands** | 5550–750, 750–1000 $cm^{-1}$ (in-plane C–H bending), 2700–3200 $cm^{-1}$, 3100 $cm^{-1}$ ($CH_4$), 2080–2220 $cm^{-1}$ (CO) | 50–750, 800 $cm^{-1}$ (=CH bending), 1037/1094 $cm^{-1}$ (=CH bending/stretching), ~1300 $cm^{-1}$ ($CH_2$ stretching), 2700–3200 $cm^{-1}$, 3100 $cm^{-1}$ ($CH_4$), 2080–2220 $cm^{-1}$ (CO) |
| **Peak Assignments** | 750–1000 $cm^{-1}$ bands correspond to aromatic/semiaromatic rings | 800, 1037/1094, ~1300 $cm^{-1}$ indicative of acyclic hydrocarbon structures [34] |
| **Decomposition Products** | Mainly cyclic species ($C_5H_6$, $C_5H_8$), $CH_4$; no $CH_2$ modes or saturated cyclic species ($C_5H_{10}$) | Mixture of cyclic and acyclic species ($C_5H_6$, $C_5H_8$, $C_5H_{10}$), including linear alkenes/alkanes confirmed by $CH_2$ modes |

**Table 2**

| Sample | Fe (wt%) | Co (wt%) |
|---|---|---|
| **rGO** | 3.0 | 4.2 |
| **Pd/rGO** | 22.0 | 27.5 |

٧٥٧ **Table 3**

| Ref | Method / Strategy | Precursors | Substrate / Support | Key temperature / process | Proof / Characterization | Key finding / Relevance |
|---|---|---|---|---|---|---|
| [35] | Site-selective ALD on graphene defects | Pt precursor ($MeCpPtMe_3$) + oxidant | CVD graphene | Moderate *T*, ALD cycles | HR-TEM, SEM, DFT | Pt nucleates preferentially at grain boundaries; atomic-scale defect-driven |
| [36] | Review of area-selective ALD/CVD | Various ALD/CVD chemistries | Oxides, graphene, patterned | Various, summarized | Multiple (QCM, TOF-SIMS, XPS, | Systematic overview of strategies enabling area selectivity; establishes |
| [37] | Area-selective CVD | Ru precursors | Patterned oxide/Si surfaces | Controlled deposition *T* | XPS, AFM, QCM | Demonstrated temperature- and chemistry-dependent |
| [27] | Sequential selective CVD (Ru–Ni core–shell | Nickelocene + Ruthenocene | Ni/rGO | Defined sequential windows | GC, TEM, XRD | Selective Ru deposition on Ni/rGO; confirmed catalytic benefit (propane |
| [38] | Site-selective CVD on 3D nanoarchitectures | Metal-organic CVD precursors | 3D direct-write nanostructur | Process specific; nanoscale | SEM, TEM | Showed site-specific CVD growth on complex architectures; expands |
| [39] | Maskless area-selective CVD (beam-assisted) | Au precursors | Patterned surfaces | Localized activation (beam- | SEM, TEM | Demonstrated spatial control via beam-assisted decomposition; alternative |

٧٥٨